GEOLOGICAL SURVEY OF CANADA
OPEN FILE 6825

A Magnetotelluric Survey Across the Committee Bay Block and Rae Craton in the Churchill Region of Nunavut

J.E. Spratt, D.B. Snyder and J.A. Craven

2011

Natural Resources Canada | Ressources naturelles Canada

Canada

GEOLOGICAL SURVEY OF CANADA
OPEN FILE 6825

A Magnetotelluric Survey Across the Committee Bay Block and Rae Craton in the Churchill Region of Nunavut

J.E. Spratt, D.B. Snyder and J.A. Craven

2011

doi:10.4095/

This publication is available from the Geological Survey of Canada Bookstore (http://gsc.nrcan.gc.ca/bookstore_e.php).
It can also be downloaded free of charge from GeoPub (http://geopub.nrcan.gc.ca/).

Recommended citation
Spratt, J.E. et al., 2011. A magnetotelluric survey across the Committee Bay block and Rae craton in the Churchill region of Nunavut; Geological Survey of Canada, Open File 6825, 28 p.

Table of Contents

Introduction

As part of Natural Resource Canada's GEM (Geo-mapping for energy and minerals) program, the Diamonds project is designed to study the deep lithosphere beneath the Slave and Churchill provinces of northern Canada with the aim of understanding the potential for diamonds and reduce the risk in their exploration. To aid in these objectives, it has been proposed to acquire long period and broadband magnetotelluric (MT) data along 5 separate corridors throughout Nunavut and the Northwest Territories over the 2010, 2011, and 2012 field seasons. During the summer of 2010, MT data were collected along a 300 km-long transect, the Diamonds I MT corridor, that extends from southwest of Repulse Bay to the south end of the Boothia Peninsula, through a portion of the Rae craton in the Churchill Province of the eastern Canadian Shield. These data will enhance and complement interpretations of previous MT data collected along the Melville Peninsula, Baffin Island, and Southampton Island, with the long term goal of generating a regional 3-dimensional conductivity model of the lithosphere (Figure 1). The data have been processed using modern, robust, remote-referencing methods and have been analyzed for dimensionality, effects of distortion, and geo-electric strike angles. Preliminary models have been derived along the 2-D profile.

Data Acquisition and processing

Prior to field operations, the MT equipment was tested, calibrated, and packed for shipment to Repulse Bay. A test site was installed in order to gain familiarity with the instrumentation, to test the interface software, and to compare the various processing codes available. The field campaign tool place from mid-July to mid-August and was based partly out of the community of Repulse Bay and partly out of the Diamonds North exploration camp, Amaruk, near Kugaaruk. Data were acquired at 17 site locations, 15 of which were located along a 2-D profile between the Archean Repulse Bay block to the southeast, through the Committee Bay block towards, but not reaching, the Queen Maud block to the northwest (Figure 2**)**. The profile crosses belts of northeast-to-southwest trending metamorphosed

sedimentary and volcanic rocks of the Prince Albert Group dated at 2.78 – 2.71 Ga (Skulski et al., 2002) and crosses a kimberlite field at its northern end known to bear diamonds. Additional data were collected at two locations north and northeast of Repulse Bay in order to provide a link between this Diamonds I profile and the Melville Peninsula MT profile collected in 2009 and to fill large gaps in future regional 3-dimensional modeling.

Long-period (LMT) data were collected at 7 site locations using NiMS recorders. Electrical fields were recorded in two horizontal, perpendicular directions using lead-lead-chloride porous pots and the magnetic fields were recorded in the vertical and two horizontal directions using a 3-component fluxgate magnetometer. Recording times and locations for each site are shown in Table 1. Data were acquired continuously for 12 – 14 days with one exception. At site DMN004, likely due to instrumentation error, no data was retrieved after the first visit to the site and total data acquisition time at that site is only 1.9 days. The data from each site were converted from the recorded binary format to ASCII format using John Booker's nimsread2ts code (Booker, *pers comm*. 2010) and the different runs were then spliced together to form one continuous time series. These long-period MT data were processed using the multi-remote-reference, robust, cascade decimation code of Jones and Jödicke (1984), generating apparent resistivity and phase response curves as a function of period, in the TE- (transverse electric) and TM- (transverse magnetic) modes, for each site. In general the data quality is good with smooth response curves and low error bars in the period range of 10 – 10,000 s (Figure 3a).

Broadband (BBMT) data were collected at a total of 17 site locations, including at the seven long-period locations, using Phoenix Geophysics recording instruments and sensors. Here the two horizontal perpendicular magnetic fields were recorded using two separate MTC50 Phoenix coils, and the vertical fields were recorded using either a MTC30 Phoenix coil, or an air loop. Data were acquired for a minimum 18 hours up to a maximum of 3 days (Table 1). The broadband data were processed from time series to response functions (apparent resistivity and phase curves) using robust remote reference techniques (Method 6 in Jones et al., 1989), as implemented by the Phoenix Geophysics software package MT2000.

This processing yielded high quality apparent resistivity and phase response curves in the period range of 0.004 – 1,000 s for most sites along the profile (Figure 3b). At locations where both long period and broadband data were collected at the same site, the response curves were merged together to generate one file with a period range of 0.004 – 10,000 s, spanning nearly 8 decades (Figure 3d).

In the northern half of the profile, thick sequences of conductive clay blanket a large portion of the region. This appears to cause a distortion effect at the shortest period ranges, resulting in a significant drop in the resistivity values and phases that go below 0° (Figure 3c). In addition to 3-dimensional galvanic distortion effects at the short periods, this will likely cause static shift effects over the whole period range that will have to be accounted for in the modeling stages. This can be done either by activating a static shift inversion parameter or by placing large error floors on the apparent resistivity, forcing the models to fit the phases preferentially.

Decomposition Analysis

Groom-Bailey decomposition techniques were applied to each site in order to understand the degree of dimensionality, determine the most appropriate geoelectric strike direction where data are deemed 2-dimensional, and ascertain and remove the effects of galvanic distortion in the data (Groom and Bailey, 1989). Single site decompositions were applied to each of the sites using the method described in McNeice and Jones (2001). At frequencies where the phase difference between the TE- and TM-modes is minimal (<10°) the data can be considered 1-dimensional, or independent of the geo-electrical strike angle. Where the phase difference is larger, the data are more dependent on the strike angle and 2-D models need to be inverted at the appropriate geo-electric strike angle in order to accurately represent the subsurface conductivity structure. At short periods, where the fields are penetrating only the top few kilometers, geo-electric strike usually follows geologic trends and these trends can be used to resolve the 90° strike ambiguity that is inherent in the analysis. Ideally a model can be generated along a profile at one strike angle for all periods;

however, where the subsurface structure is complex and this angle changes along profile or with depth, the profile may need to be divided into sections and modeled separately at the different geo-electric strike angles. In some cases, no strike angle can be found that fits the data with a reasonable RMS misfit (< 2) even with no bandwidth constraints. This situation was observed at short periods at some sites, particularly at the northwestern end of the profile. Along with large RMS values, the data show highly inconsistent twist or shear values, variables that describe galvanic distortion (Figure 4). These variables suggest that the subsurface may not be accurately represented with a 2-D model and that short period data at these sites may need to be omitted.

The strike directions resulting from single site, single-decade bandwidth decompositions using a 90° ambiguity and an error floor set to 3.5%, equivalent to 2° phase, are shown in Figure 5. Below 0.1 s most of the sites show low phase differences with a few exceptions. These exceptions show a large degree of scatter in the geo-electric strike angle suggesting that local structures are influencing the data. Apart from the southwestern-most sites, most of the sites in the southern half of the profile have small phases differences (<10°) over the majority of the period range and can be considered 1-D, indicating a layered subsurface. Although the phase differences are low, the preferred geo-electric strike angle is fairly uniform with values of 50 – 60° that are consistent with the regional geologic trend (Figure 6). This strike probably corresponds to data recorded in the TE-mode, oriented parallel to geo-electric strike direction.

The northwestern half of the profile generally exhibits higher phase differences (illustrated by the red ellipses in Figure 5) where any 2-D models will be strongly dependent on the strike angle selected. This indicates that more complex subsurface structure exists than that further to the southwest. Maximum phase differences are observed between 0.1 and 1000 s, where there appears to be a change in the geo-electric strike angle from 20 – 35° at periods <10 s to 50 – 60° at periods >10 s. As the depth of penetration is dependent on both the period and resistivity of the subsurface, this depth at a particular period may be different from one site to the next. In general, basic depth estimates show that periods <10 s roughly

correspond to crustal depths (<40 km) whereas periods >10 s are likely penetrating into the upper mantle (>40 km). The strike angle of 20 – 35°, likely occurring in the lower crust, is inconsistent with the regional geologic trend and aeromagnetic trends and cannot be easily explained by local structure. This causes uncertainty in discerning the 90° ambiguity and in assigning the TM- or TE-mode to this strike angle. The northeastern-most sites indicate a weak preference of ~70° for periods of 10 – 1000 s, consistent with the plate motion vector and thus likely representing TE-mode data (Figure 7). At periods greater than 1000 s, the phase splits are <10° at all sites, and the data can be considered 1-D.

The data were recalculated at strike angles of 24°, 55°, and 70°. Figure 7 shows the misfit values for the whole period range at each site. A misfit value of < 2 indicates that a 2-D model of the earth at that strike angle could be adequately represented by the data. The decompositions from site DMN002 through to site DMN014 show a good fit to the data at all three of the selected strike angles. The geo-electric strike angle that best fits most of the sites over most of the period ranges is 55°. Three sites appear to be strongly influenced by the strike angle selection: sites DMN001, DMN004, and DMN016. The northwestern-most 2 sites and the long periods at site DMN016 show a preference for a strike of 70°, whereas at short periods and sites DMN016 and DMN001, there is a preference for a strike of 24°. Site DMN004 shows a high misfit to the data at any strike angle selected, an indication of 3-dimensional effects on the data. Two-dimensional models will next be generated with the data recalculated at each of the three angles to understand better how a change in the strike angle will effect the resulting conductivity structure. Models will also be generated with and without site DMN004 to assess how this data effects the conductivity structure and the misfit value of the model to the data.

Depth estimates

Rough estimates of penetration depths were determined using Schmucker's c-function analysis, which calculates the depth of maximum eddy current flow (Schmucker, 1970). These estimates indicate that the data at most of the sites penetrate to > 200 km depths, and

in some cases to > 350 km (Figure 8). These penetration depths are sufficient to image the deep lithosphere of the Earth beneath the profile.

Non-uniform source fields

Non-uniform source field effects, due to the auroral electrojet, often cause distortion on MT data collected at high latitudes. The distortion is typically seen as reduced apparent resistivity values, and increased phase values at long periods, and can cause the depth to asthenosphere to be underestimate by nearly 50 km (Jones and Spratt, 2002). Analyses using the method described in Jones and Spratt (2002) were applied to several of the long-period sites and had no noticeable effect on the response curves. This suggests that there was little such effect on the long period data.

Ocean effects

It is know that the presence of sea water, a near-surface 3-dimensional highly conductive body, can have significant effects on MT data, primarily due to the sharp contrast in resistivity between the land and the ocean (Schmucker, 1970, Menveillie et al., 1982). Coastal effects are preferentially observed in the long-period data. The severity of these effects is dependent on the salinity of the sea water, the conductivity structure of the subsurface, the depth of the ocean, and the proximity of the MT site to the coast (e.g., Jones, 1981; Santos et al., 2001; Pous et al., 2003). In order to assess the coastal effects on this data set, a 3-D mesh was created with ocean resistivity values of 0.3 ohm-m extending to depths of 500m, (approximated from the International Bathymetric Chart of the Arctic Ocean: http://www.ngdc.noaa.gov/mgg/bathymetry/arctic/arctic.html), and a uniform land resitivity values of 1000 ohm-m (Figure 9a). Forward modeling then calculated synthetic response curves at the recorded site locations. This method of determining coastal effects is approximate because: the coast line is not exact, the depth and resistivity of the ocean is approximated, and a uniformly resistive earth used rather than a layered or structured earth.

This estimate is therefore only used to illustrate caution in interpreting 2-dimensional models that include long period data near the coast.

The calculated forward response curves show little effect of the ocean on the northermost sites (Figure 9b; the calculated apparent resistivity and phase curves are consistent with that of a uniform half space of 1000 ohm-m. The strongest effect is seen at sites DMN001 and DMN018 (Figures 9c and 9d), at a period of roughly 100s, however, some effect is noted at site DMN018 as early as 10 s. Depth analysis, similar to that described above, for site DMN018 shows that 10 s corresponds to a depth of ~ 100 km. Depth analysis of site DMN001 shows that 100 s in the XY mode (the recorded north-south direction) corresponds to depths of ~ 300 km suggesting that a conductivity model of lithosphere should be relatively unaffected by the ocean effects.

Data Modeling

The distortion-corrected, regional 2-D responses from sites along the main northwest to southeast profile were imported in the WinGlink MT interpretation software package as three separate projects, each assuming a geo-electric strike angle of 24°, 55°, and 70°, respectively. A fourth project was generated for the data with the TM-mode assigned to 24°, effectively a geo-electric strike angle of 114°. Each site in each of the projects has been manually edited to remove data points with large error bars or large scatter. Additionally data that were shown to have high misfit values in the decomposition analysis, primarily data in the shortest period range, were removed. Static shift effects on the data cannot be numerically determined. Typically, static shift effects arise from a charge build up at the base of near surface conductors and the effect is to raise the apparent resistivity values of the entire response curve. Where one apparent resistivity curve of one mode was much higher than the other, that curve was reduced to match the other curve at the shortest period. This helps to reduce the effect of anisotropic shift, but does not account for the cases were both curves are affected by static shift.

1-D Models

One-dimensional layered earth models were generated for each site using Occam's inversion codes as implemented by the WingLink MT interpretation software package and were stitched together to form cross-sections along the Diamonds I MT corridor (Figure 10a). Pseudosections of the phase responses for each of the sites along the profile were generated for both the TE- and TM-modes (Figures 10b). As previously described in the phase difference plots, where these sections are similar, the 1-D models can be considered to be a valid representation of the Earth; however, they do not account for static shift effects. The dashed red box in figure 10, shows the area where the data are predominantly 1-D and the stitched 1-D models show a laterally uniform layered Earth. The data outside the red box, show much more complex structure requiring 2-D, or 3-D modelling.

Variations with strikes

As is common with many regularized inversion codes, this 2-D code searches iteratively for the smoothest model that best fits the data by attempting to trade off the fit to the observed data (data misfit) with the squared Laplacian (smoothing term) of the horizontal and vertical resistivity gradients. The inversion program searches for the smoothest, best-fit model with the least deviation from the starting model, which is usually a half space (Mackie and Madden, 1993). This means that the resultant models represent the minimum structure required to fit the data with an acceptable misfit.

Many different models need to be generated using various combinations of modes and parameters in order to observe the effects of these changes on the model structure and to derive the most robust final model with an appropriate misfit value. In an attempt to determine the most appropriate parameters for this data set, several models were generated using different data components and parameters at each of the different strike angles (Figure 11). The inversions were initiated with a homogeneous half space of 500 ohm-m, a mesh consisting of 60 rows and 151 columns, and a smoothing parameter (tau) of 15. The phases were set with a 2° error floor, determined from the acceptable misfit values obtained in the

distortion analysis, and the apparent resistivity error floor was set to 30% to account for static shift effects. Variable parameters include: using combinations of the TM and TE mode data, the smoothing parameters alpha and beta that trade-off vertical against horizontal gradient weighting, and the weighting of the regularization order.

Regardless of the data component or smoothing variables applied, the model at a strike angle of 55° always resulted in the lowest RMS value. This strike angle is thus most appropriate for representing the whole profile. Differences between the models at different strike angles occur predominantly at the northwestern end of the profile (Figure 11 i-p), both in the shallow upper crustal structure and in the deep upper mantle structure. These differences can be addressed by modeling this section of the profile separately using the short period data at the appropriate 24° strike angle and the long period data at 70°. When inverting fewer data the responses to local-scale structures have a greater influence on the average misfit value and are better represented in the models.

Tau vs RMS plot

Several models were generated from the data at a geo-electric strike angle of 55°, using the entire period range of 0.004 – 10,000 s of both the TM- and TE-modes. The error floors were set to 30% for the apparent resistivity to account for static shift effects, and 7% for the phase. For each model the smoothness parameter, tau, was changed after 100 iterations in order to determine the most appropriate tau value for the dataset. Figure 12 illustrates the trade-off between the roughness of the model, defined by the tau parameter, and the fit of the model to the data, RMS. This shows that a tau value of 7 would result in the smoothest model with the best fit to the data.

Preliminary models

Although these models represent rough preliminary conductivity images, some features appear to be consistent in the data (Figure 11). The models show a resistive crust to depths of ~20 km that is underlain by a less resistive lower crust. This is inconsistent with

the results along the Melville peninsula that show high resistivities to depths of 35 – 39 km. All of the models show a change from laterally continuous layers to a more complex structure that is observed at crustal depths in the vicinity of the diamond-bearing kimberlite field at the northwestern end of the profile. Focussed inversions of this region may help to reveal the subsurface features and provide information on these kimberlites. The models also show a resistive upper mantle and an decrease in resistivity at depths ranging between 150 and 250 km. Additional modeling is required to constrain the depth of this change and its lateral continuity, but it may represent the boundary between a resistive lithosphere and a conductive asthenosphere or to metasomatism within the deep mantle lithosphere.

Conclusions

Careful processing and analysis of MT data collected along the Diamonds I MT corridor have provided a good understanding of the dimensionality and distortion of the data and show that the quality of the data is sufficient to model the lithospheric conductivity structure beneath the profile. Decomposition analysis shows that a geo-electric strike angle of 55° is appropriate for most of the data at most of the period range and that a strike of 24° and/or 70° should be considered for a section at the northwestern end of the profile. Systematic modeling of the data at different strike angles using different variables has helped to determine some of the inversion parameters that should be used to provide an accurate image of the subsurface. Preliminary 1-D and 2-D models reveal some structure that appears to be consistent in the data. These models also illustrate the need for additional 2-D and 3-D inversions required to further resolve the subsurface conductivity structure.

References

Groom, R.W., and R.C. Bailey, 1989: Decomposition of magnetotelluric impedance tensors in the presence of local three-dimensional galvanic distortion; Journal of Geophysical Research, v. 94, p. 1913 – 1935.

Jones, A.G., 1981: Geomagnetic Induction Studies in Scandinavia - II. Geomagnetic Depth Sounding, Induction Vectors and Coast-Effect; Journal of Geophysics, v.50, p. 23 – 36.

Jones, A.G., and H. Jodicke, 1984: Magnetotelluric transfer function estimation improvement by a coherence-based rejection technique, paper presented at the 54th Society of Exploration Geophysics Annual General Meeting, Atlanta, George, 2-6 December, Abstract volume, pp. 51-55.

Jones, A.G., and J.E. Spratt, 2001: A simple method for deriving the uniform field MT responses in auroral zones; Earth and Planetary Science Letters, v. 54, p. 443 – 450.

Jones, A.G., A.D. Chave, G.D. Egbert, D. Auld, and K. Barh, 1989: A comparison of techniques for magnetotelluric response function estimation; Journal of Geophysical Research, v. 94, p. 14210 – 14213.

Mackie, R.L., and T.R. Madden, 1993: Three-dimensional magnetotelluric inversion using conjugate gradients; Geophysical Journal Internations, V. 115, p. 215 – 229.

McNeice, G.W., and A.G. Jones, 2001: Multisite, multifrequency tensor decomposition of magnetotelluric data; Geophysics, v. 66, p. 158 – 173.

Menvielle, M.J.C., P. Rossignal, and P. Tarits, 1982: The coast effect in terms of deviated electric currents: A numerical study; Physics of the Earth and Planetary Interiors, v. 28, p. 118 – 128.

Pous, J., W. Heise, P.A. Schegg, G. Munoz, J. Mart, and C. Soriano, 2002: Magnetotelluric study of the Las Canadas caldera (Tenerife, Canary Islands): structural and hydrogeological implications; Earth and Planetary Science Letters, v. 204, p. 249 – 263.

Santos, F. A. M., M. Nolasco, E. P. Almeida, J.Pous and L.A. Mendes-Victor: 2001. Coast

effects on magnetic and magnetotelluric transfer functions and their correction: application to MT soundings carried out in SW Iberia; Earth and Planetary Science Letters, v.186, p. 283-295.

Schmucker, U., 1970. Anomalies of geomagnetic variations in the southwestern United States, Bull. Scripps Ints. Oceanogr. v. 13, 165 p.

Skulski, T., Paul, D., Buckle, J., Sandeman, H., Berman, R., Pehresson, S., Rainbird, R., Davis, W., Kerswill, J., and Sandborn-Barrie, M., in prep. Bedrock geology and regional synthesis of the north-central Rae domain, western Churchill Province, Nunavut, Canada; Geological Survey of Canada, Open File 5577, 1:5500,000 scale.

Site Name	Data Range	Latitude	Longitude	Start Date	Start Time	End Date	End Time	Duration of acquisition
DMN001	LMT	65.9790	-87.2700	16/07/2010	13:00	29/07/2010	08:30	12.8 days
DMN004	LMT	66.3666	-88.0419	17/07/2010	13:00	19/07/2010	10:00	1.9 days
DMN007	LMT	66.7484	-88.6810	17/07/2010	18:00	29/07/2010	11:30	11.7 days
DMN009	LMT	67.1073	-89.4056	24/07/2010	12:30	12/08/10	11:45	19.0 days
DMN014	LMT	67.8303	-90.5411	01/08/10	12:30	15/08/2010	12:45	14.0 days
DMN017	LMT	68.3168	-91.3690	01/08/10	19:30	15/08/2010	11:00	13.6 days
DMN025	LMT	68.5915	-91.9493	02/08/10	18:30	15/08/2010	10:30	12.7 days
DMN001	BBMT	65.9790	-87.2700	16/07/2010	18:00	19/07/2010	08:40	2.6 days
DMN002	BBMT	66.11	-87.56	19/07/2010	18:00	22/07/2010	08:40	2.6 days
DMN003	BBMT	66.2301	-87.7869	19/07/2010	18:00	22/07/2010	09:20	2.6 days
DMN004	BBMT	66.3666	-88.0419	16/07/2010	18:00	19/07/2010	12:00	2.7 days
DMN005	BBMT	66.5136	-88.2431	22/07/2010	12:00	24/07/2010	09:00	1.9 days
DMN006	BBMT	66.6391	-88.4988	22/07/2010	13:00	24/07/2010	09:40	1.8 days
DMN007	BBMT	66.7484	-88.6810	24/07/201	13:30	26/07/210	15:30	2.1 days
DMN008	BBMT	66.9409	-89.0388	26/07/2010	18:00	29/07/2010	12:00	2.7 days
DMN009	BBMT	67.1073	-89.4067	24/07/2010	13:00	26/07/2010	15:30	2.1 days
DMN011	BBMT	67.4855	-90.0691	08/08/2010	11:00	10/08/2010	08:45	1.9 days
DMN012	BBMT	67.6896	-90.2932	10/08/2010	11:00	12/08/2010	12:40	2.0 days
DMN014	BBMT	67.8303	-90.5411	01/08/2010	15:00	03/08/2010	17:20	2.1 days
DMN015	BBMT	67.9481	-90.7857	03/08/2010	20:00	05/08/2010	10:20	1.6 days
DMN016	BBMT	68.1095	-91.0743	05/08/2010	11:00	07/08/2010	10:30	2.0 days
DMN017	BBMT	68.3168	-91.3690	05/08/2010	12:30	07/08/2010	11:20	2.0 days
DMN024	BBMT	68.4386	-91.6248	04/08/2010	17:00	06/08/2010	08:40	1.6 days
DMN025	BBMT	68.5915	-91.9493	02/08/2010	18:00	04/08/2010	12:40	1.7 days
DMN018	BBMT	66.8650	-87.4019	26/07/2010	18:00	27/07/2010	15:20	0.9 days
DMN019	BBMT	67.0843	-86.1212	27/07/2010	18:00	29/07/2010	14:30	1.8 days

Table 1: Site type, location, and recording times for each of the MT sites collected along the Diamonds I profile.

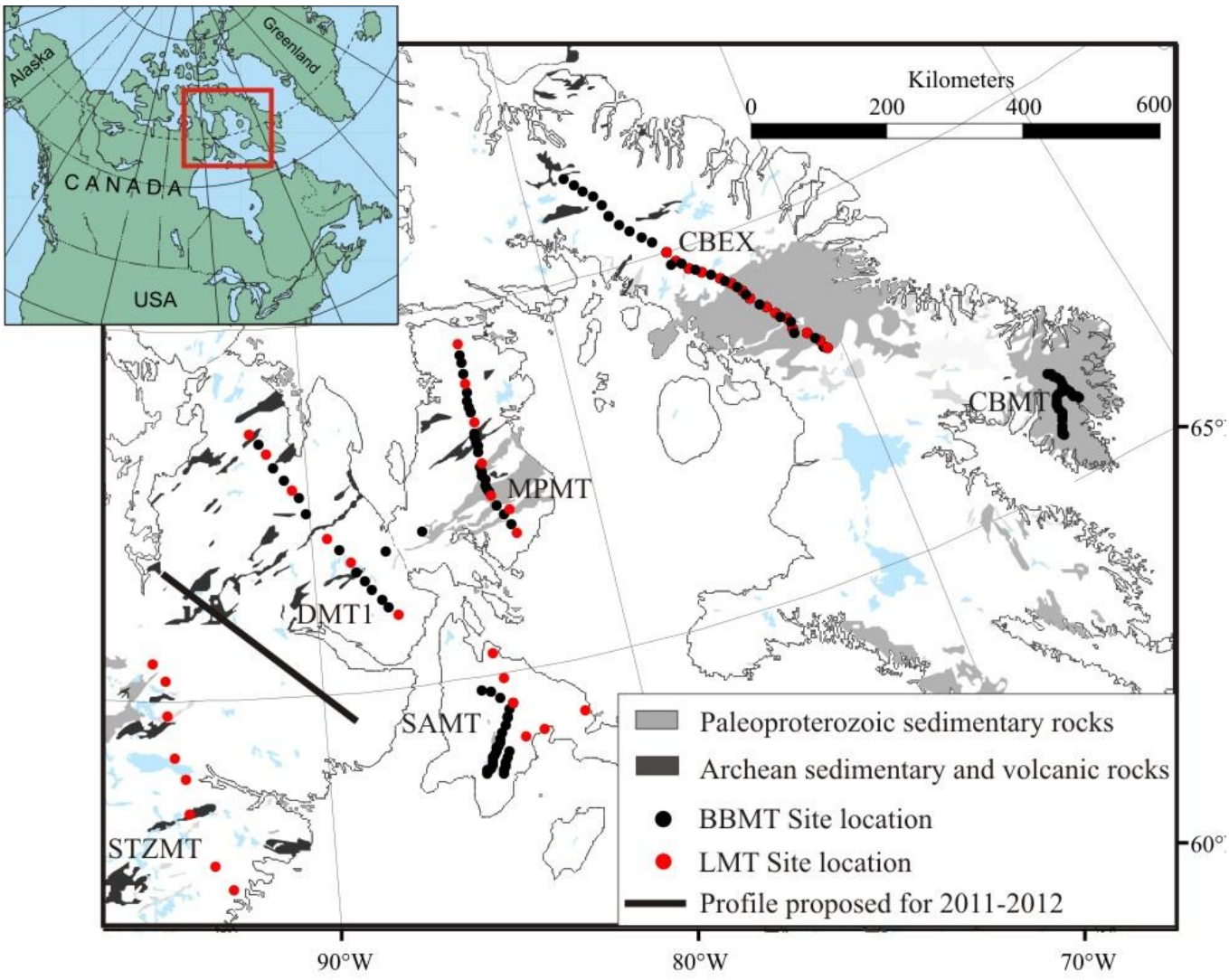

Figure 1: Regional map illustrating the locations of MT surveys in eastern Nunavut: CBEX= the Central Baffin Magnetotelluric Experment, MPMT = Melville Peninsula Magnetotelluric survey, SAMT = Southampton Magnetotelluric survey, DMT1 = Diamonds Magnetotelluric surevey: corridor 1, CPMT - Cumberland Peninsula Magnetotelluric survey, and STZMT - Snowbird Tectonic Zone Magnetotelluric survey

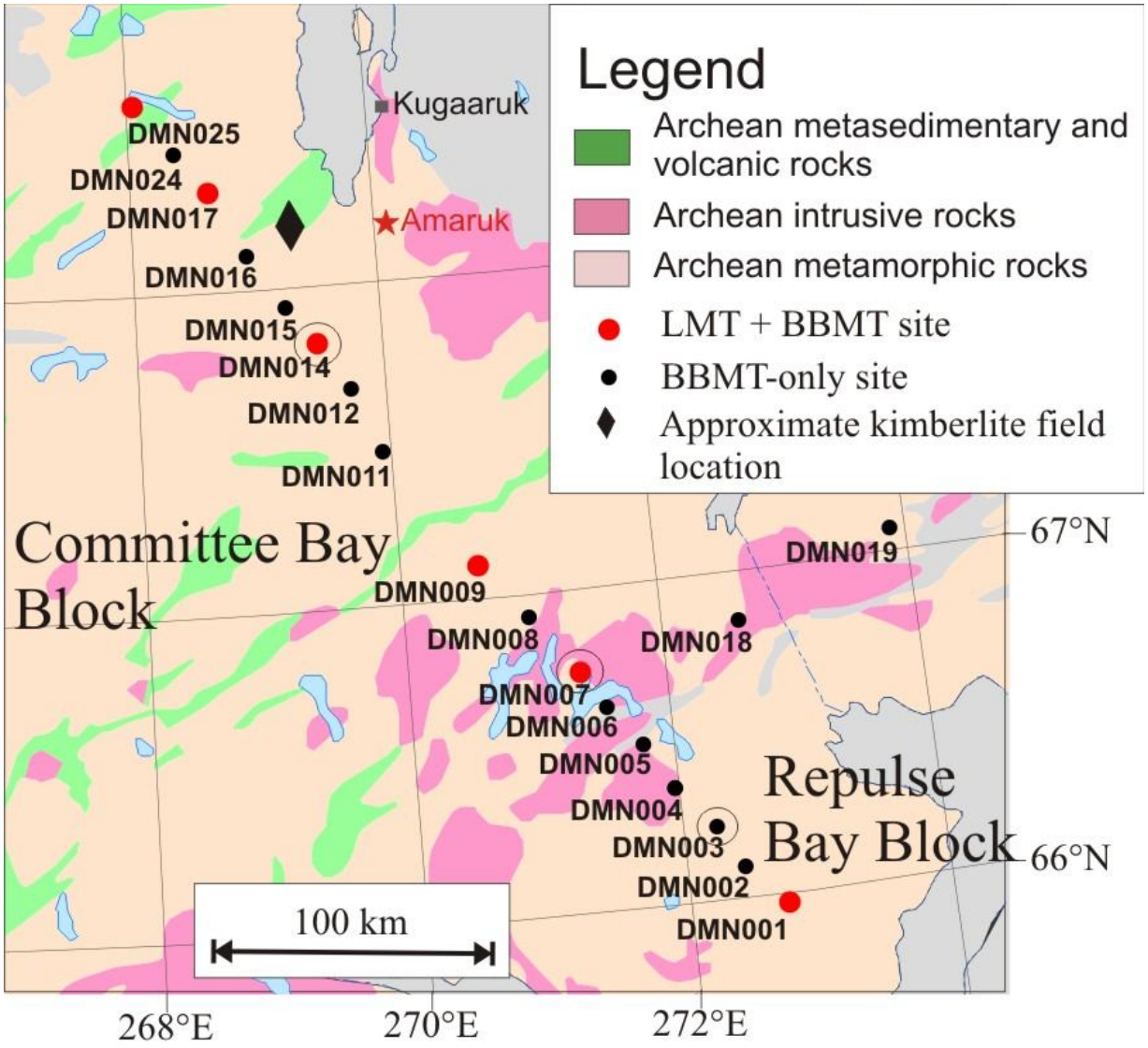

Figure 2: Geological map of the survey area showing the location of the MT sites recorded. The circles mark the location of the response curves examples shown in figure 3.

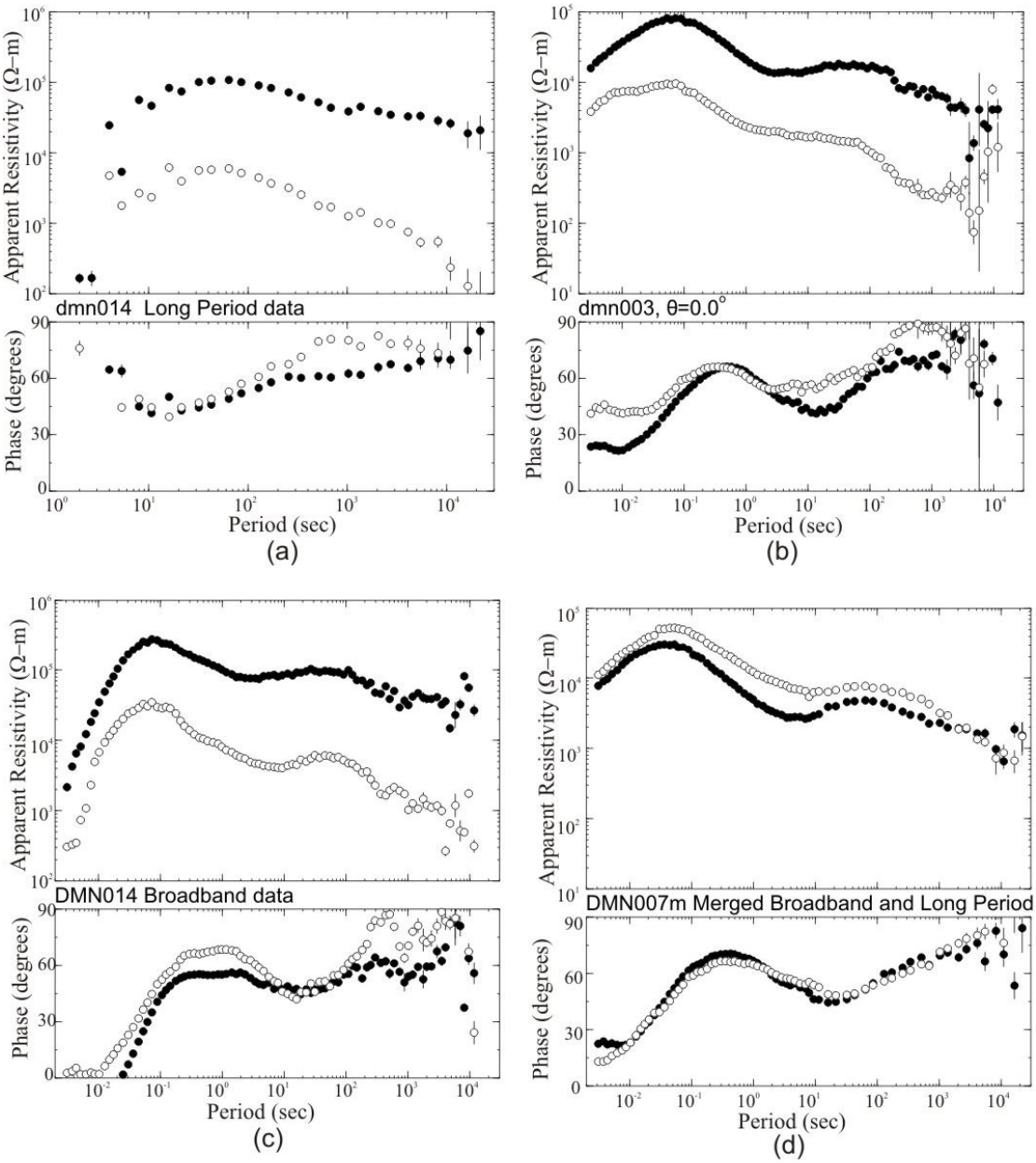

Figure 3: Examples of apparent resistivity and phase MT response curves for data measured at 3 sites: (a) shows an example of the long period data recorded, (b) shows an example of the broadband data, (c) shows an example of the short period distortion observed some sites, and (d) shows merged broadband and long period data at a site located within resistive Archean orthogneiss.

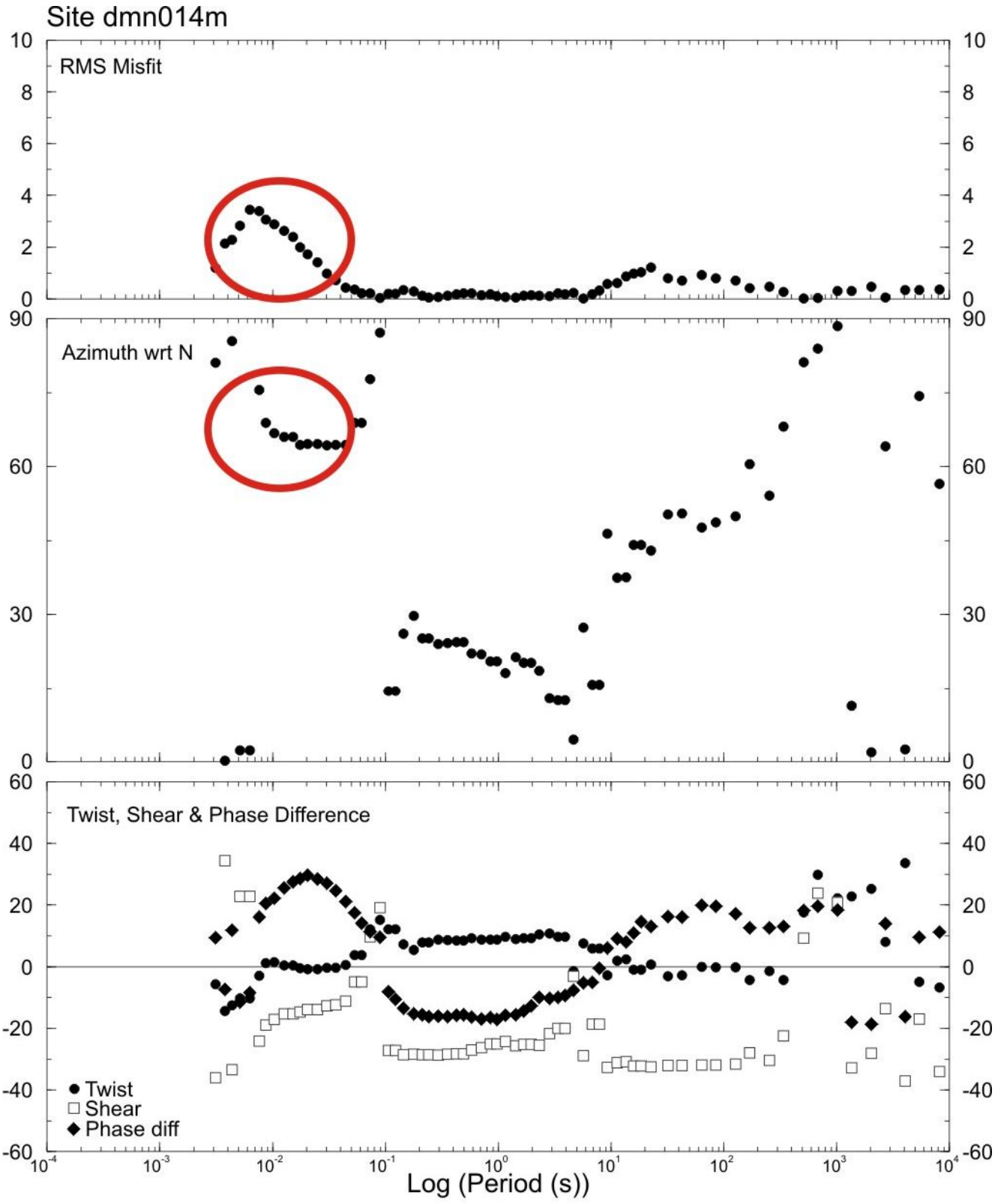

Figure 4: Example of a site showing high RMS values where no constraints are place on the data. The high RMS values correspond to high variations in the twist value suggestion the presence of local 3-d distortion.

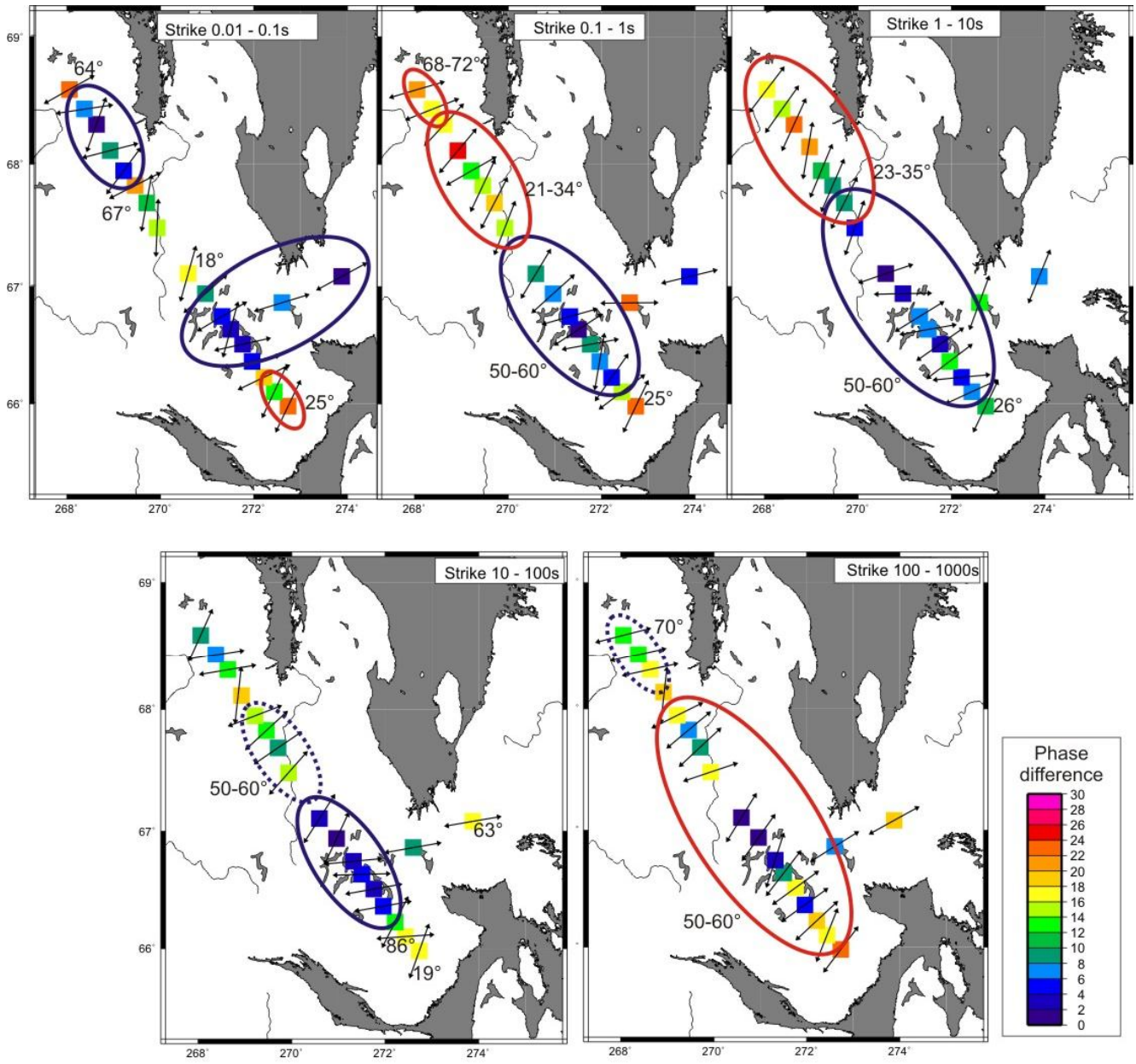

Figure 5: Maps showing the preferred geo-electric strike direction at each site along the profile for54 decade period bands. The color scale illustrates the maximum difference between the TM- and TE-mode phases. The blue ellipses show areas where the data can be regarded as 1-dimensional, the red ellipses illustrate the location and period range where the model will be dependent on the geo-electric strike angle. The dashed blue ellipses show a weak preference for a strike direction with phases differences between 10 and 15°.

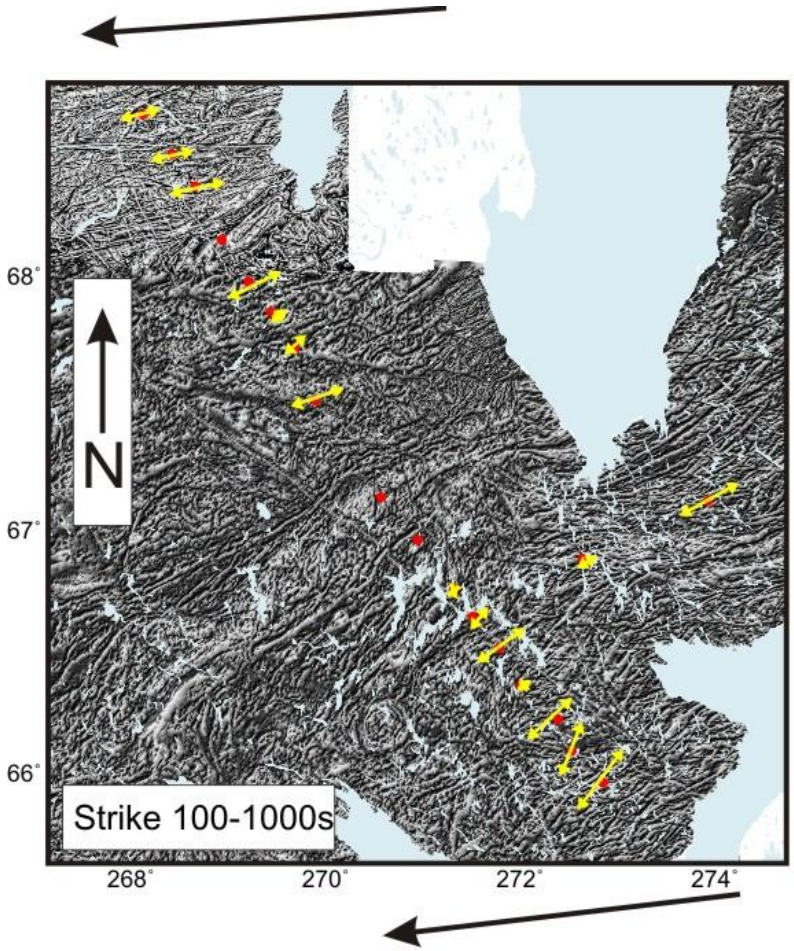

Figure 6: Map of the MT survey area showing the aeromagnetic tilt data. The yellow arrows show the preferred geo-electric strike direction at the 100 - 1000s period bandwidth, the length of the yellow arrows is scaled by the maximum phase difference between the TM and TE modes. The black arrows mark the direction of the relative plate motion vectors.

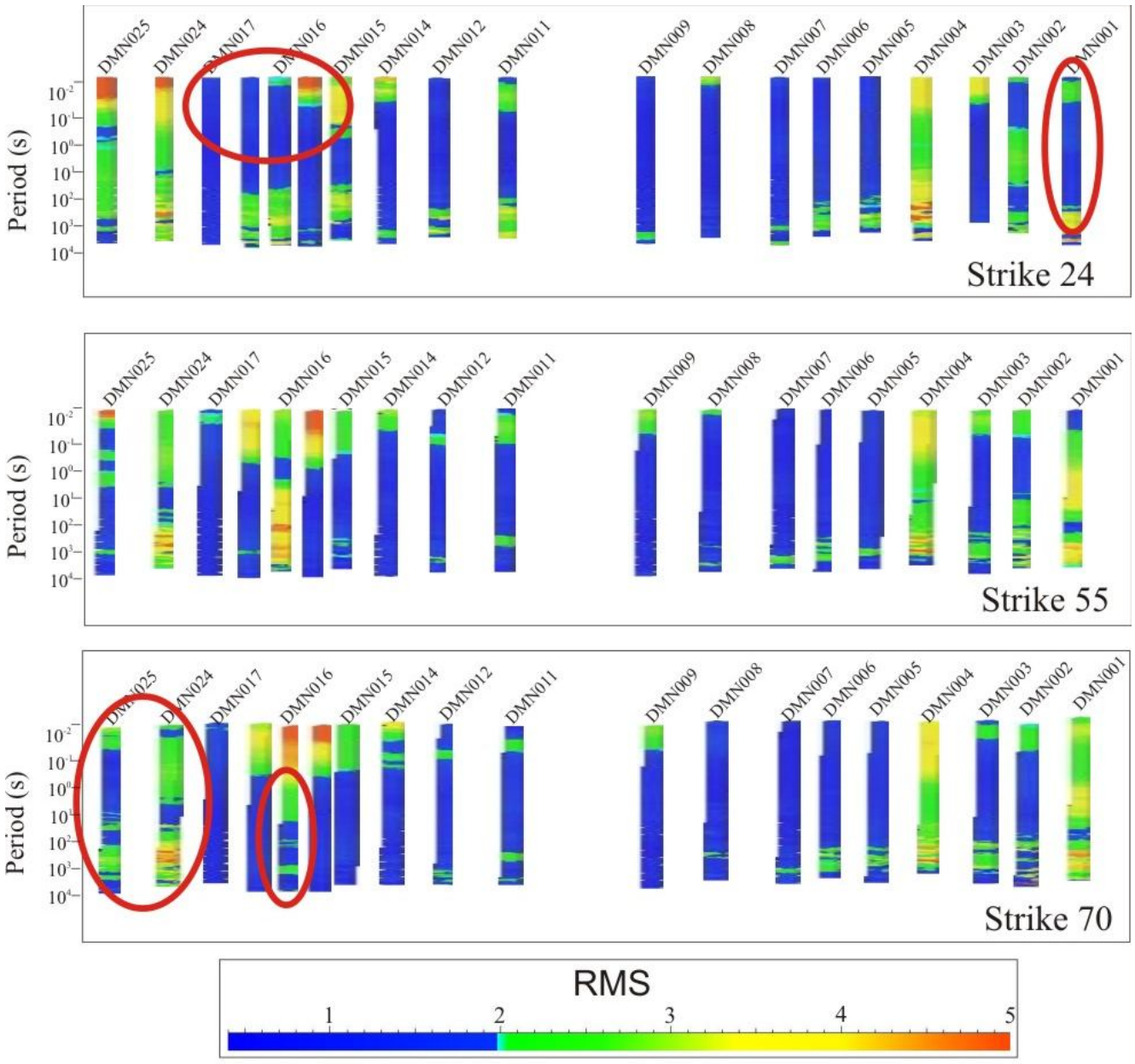

Figure 7: Data misfit values at each site over the whole recorded period range for data recalculated at a geo-electric strike direction of 24° (a), 55° (b) and 70° (c). The red ellipses mark area where there is a strong preference for a particular strike direction.

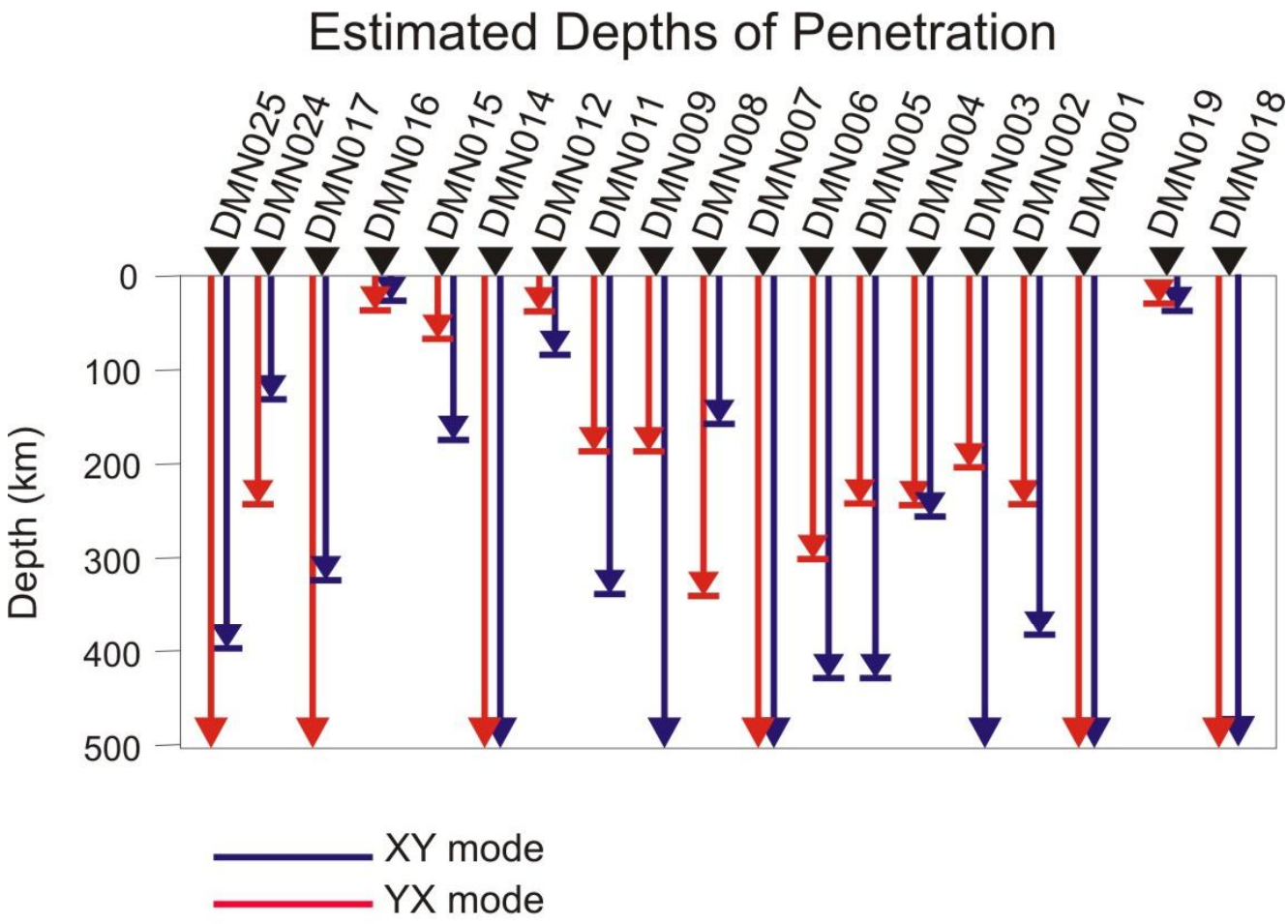

Figure 8: Estimates of maximum penetration depths for each mode at each site along the profile.

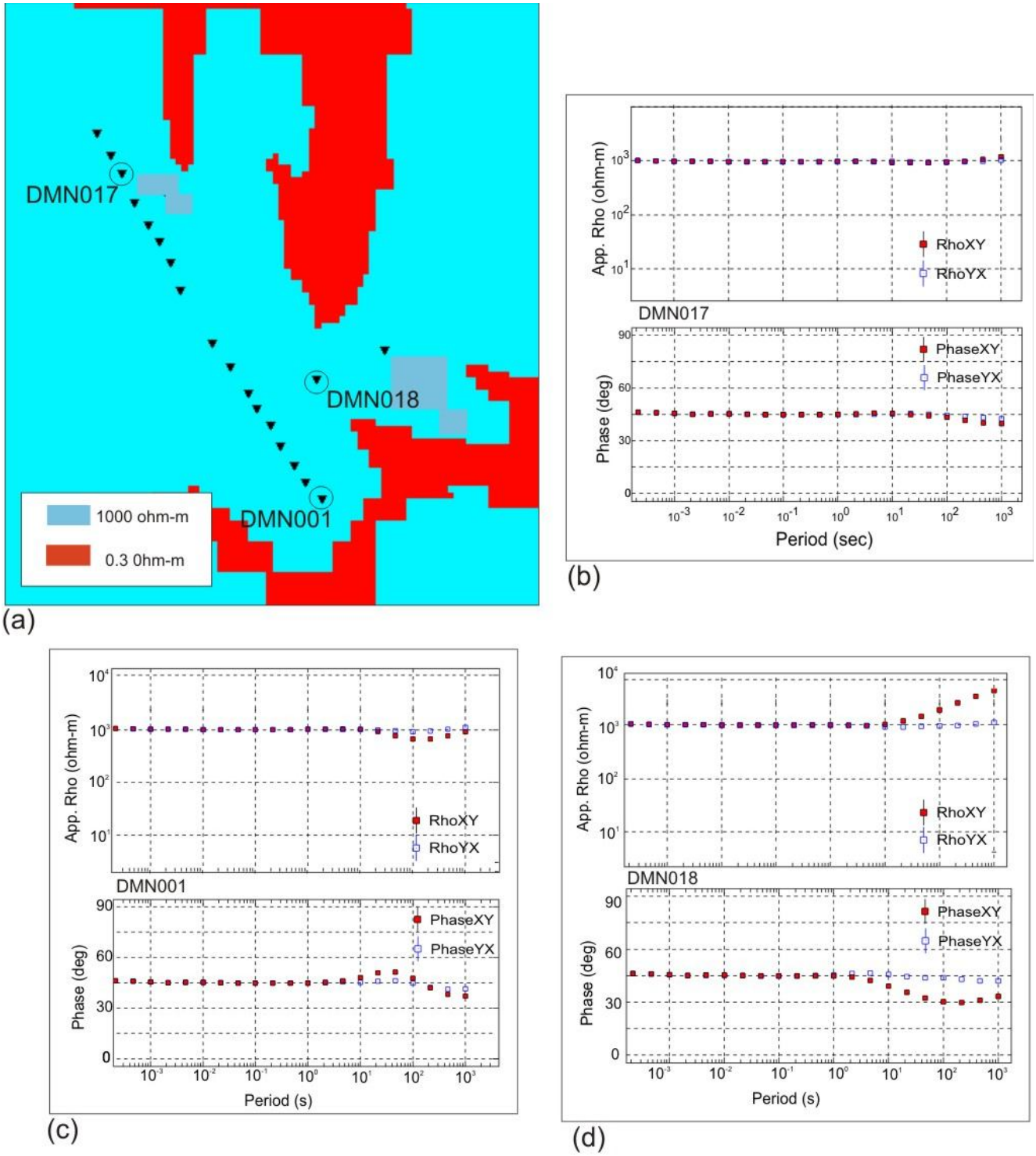

Figure 9: The 3-D mesh of the MT survey area showing the land versus ocean conductivity contrast (a). Examples of the forward calculated response curves are shown for sites DMN017 (b), DMN001 (c), and DMN018 (d).

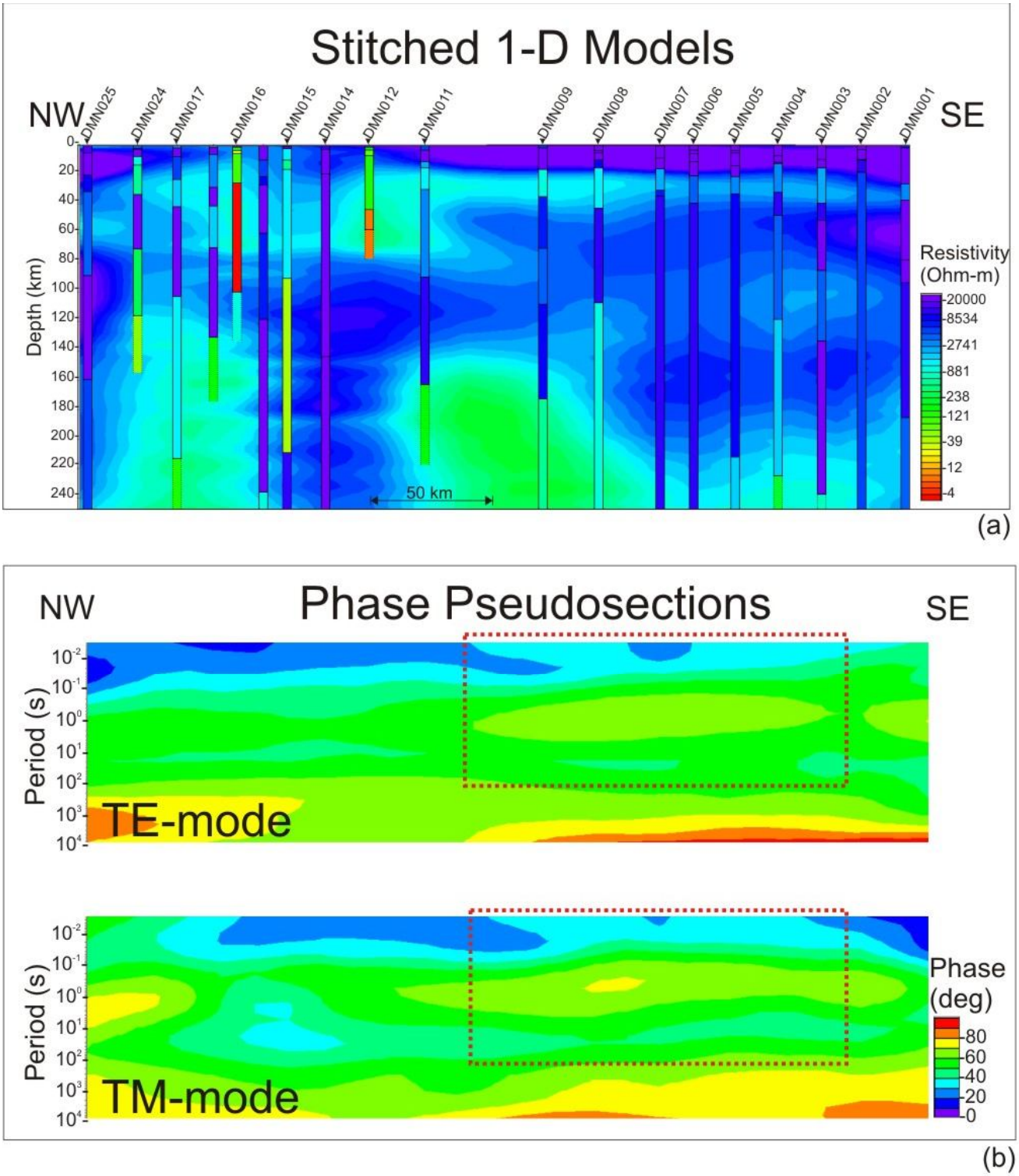

Figure 10: (a) Cross-sections along the Diamonds MT profile illustrating the results of 1-dimensional Occam inversions. (b) Pseudosections of the phases with increasing period of both the TE- (top) and TM- (bottom) modes. The red box marks the area where the data are 1-dimensional, outside this box there are significant differences between the two modes.

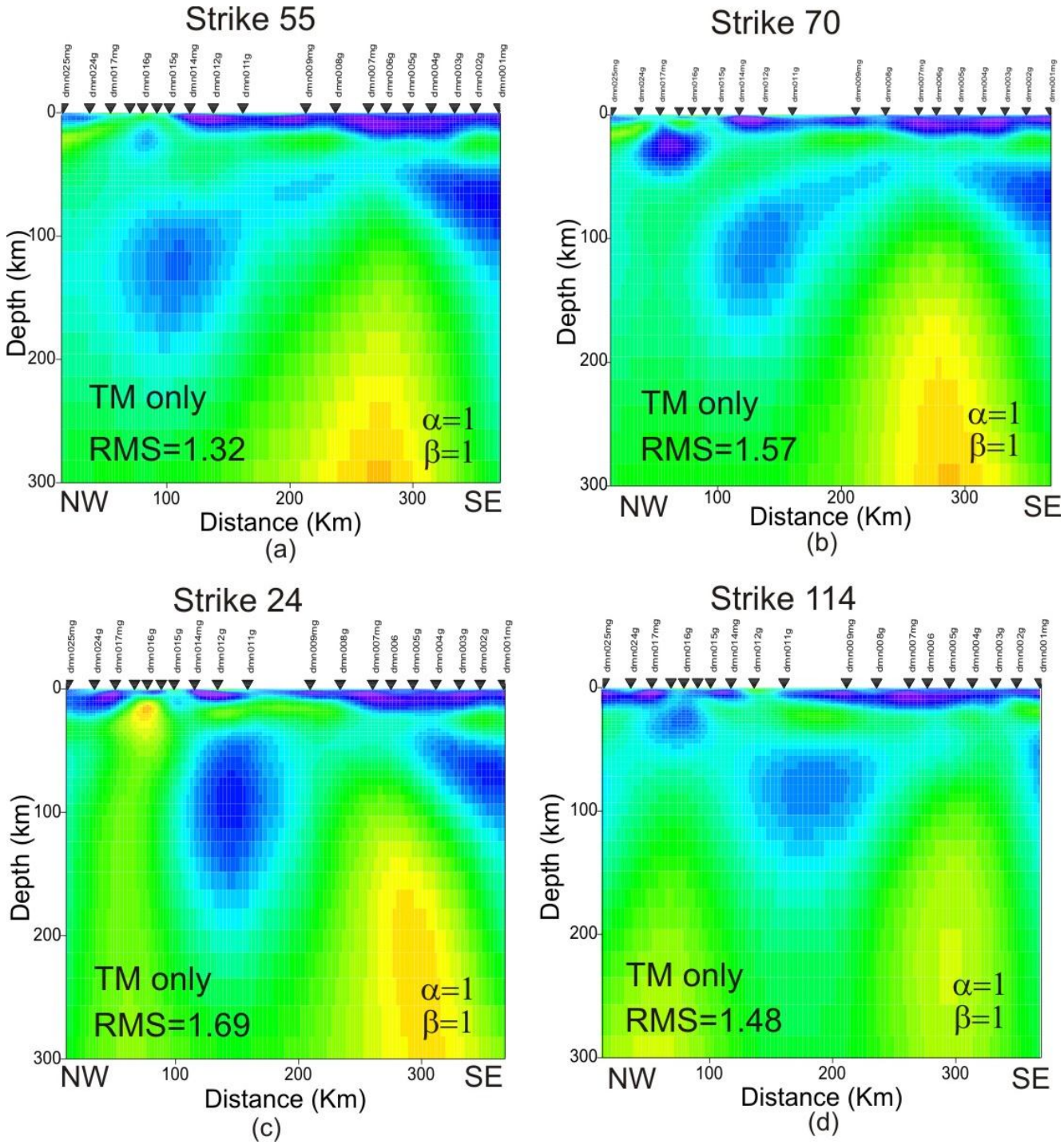
Strike 55
Depth (km)
0
100
200
300
NW
100
200
300
SE
Distance (Km)
TM only
RMS=1.32
α=1
β=1
(a)
Strike 70
Depth (km)
TM only
RMS=1.57
α=1
β=1
Distance (Km)
(b)
Strike 24
Depth (km)
TM only
RMS=1.69
α=1
β=1
Distance (Km)
(c)
Strike 114
Depth (km)
TM only
RMS=1.48
α=1
β=1
Distance (Km)
(d)

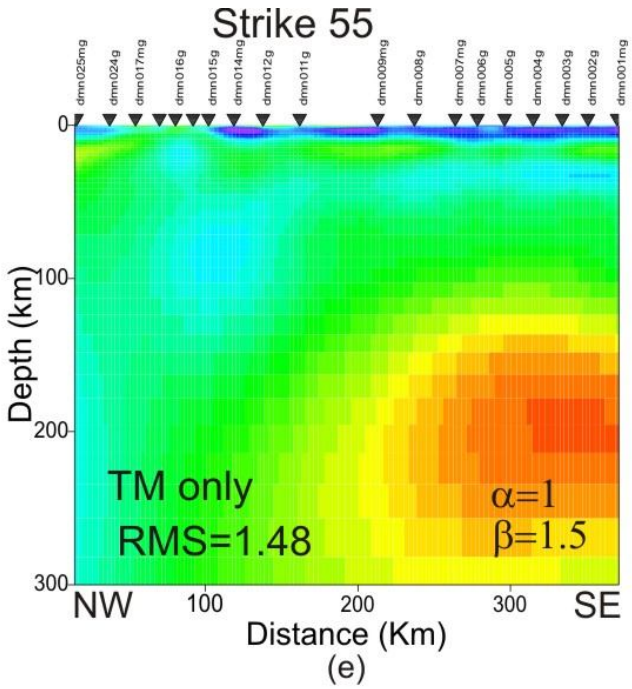
Strike 55
Depth (km)
0
100
200
300
NW
100
200
300
SE
Distance (Km)
TM only
RMS=1.48
α=1
β=1.5

(e)

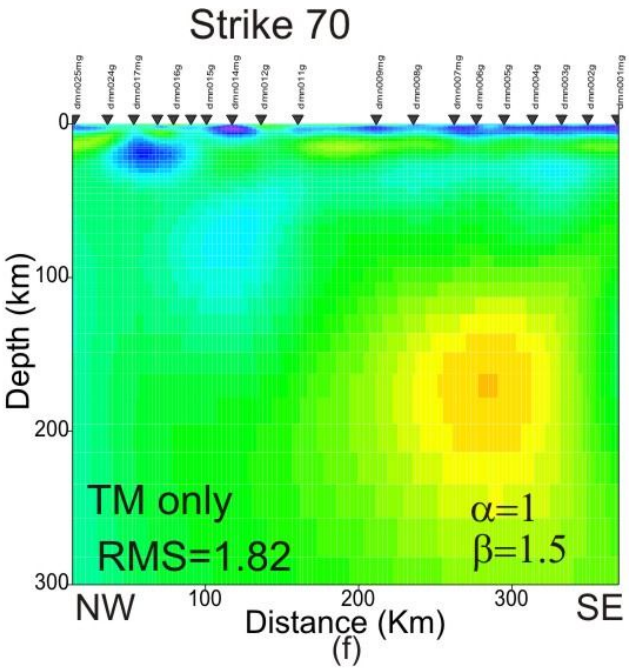
Strike 70
Depth (km)
0
100
200
300
NW
100
200
300
SE
Distance (Km)
TM only
RMS=1.82
α=1
β=1.5

(f)

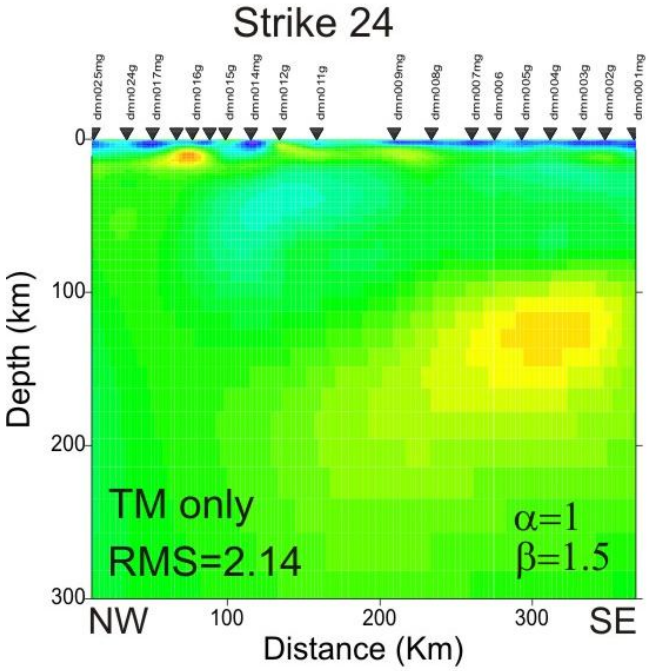
Strike 24
Depth (km)
0
100
200
300
NW
100
200
300
SE
Distance (Km)
TM only
RMS=2.14
α=1
β=1.5

(g)

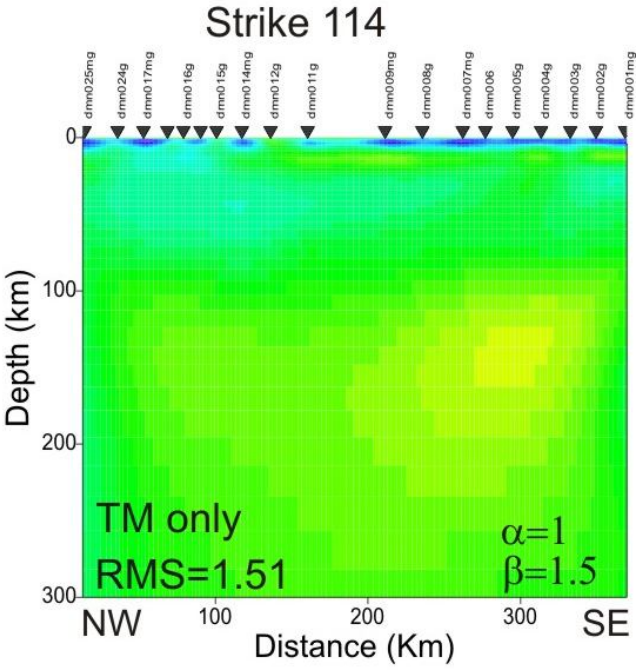
Strike 114
Depth (km)
0
100
200
300
NW
100
200
300
SE
Distance (Km)
TM only
RMS=1.51
α=1
β=1.5

(h)

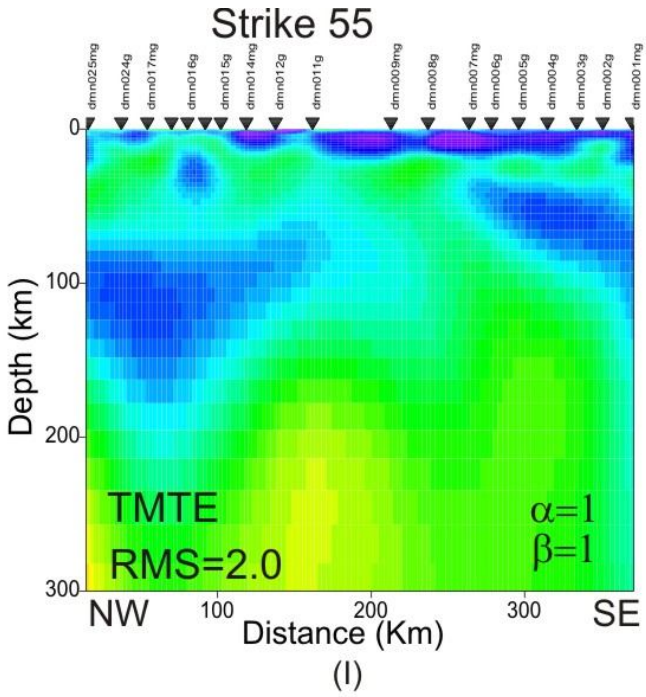
Strike 55
Depth (km)
0
100
200
300
TMTE
RMS=2.0
α=1
β=1
NW
100
200
300
SE
Distance (Km)

(l)

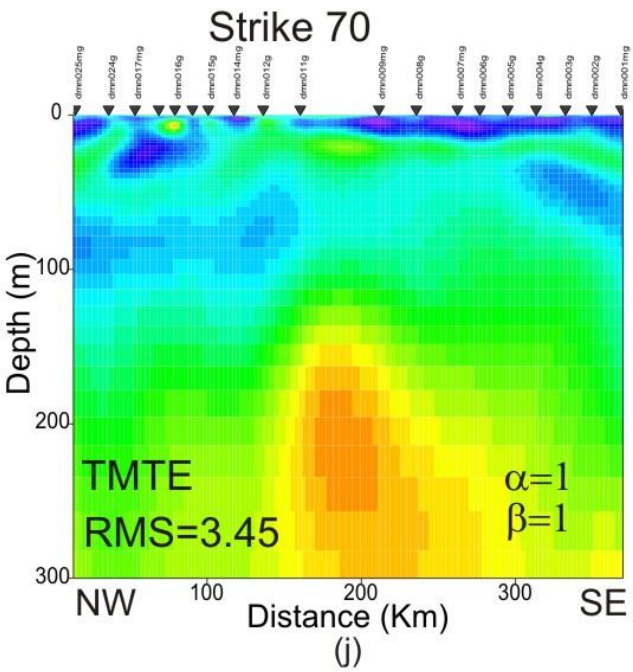
Strike 70
Depth (m)
0
100
200
300
TMTE
RMS=3.45
α=1
β=1
NW
100
200
300
SE
Distance (Km)

(j)

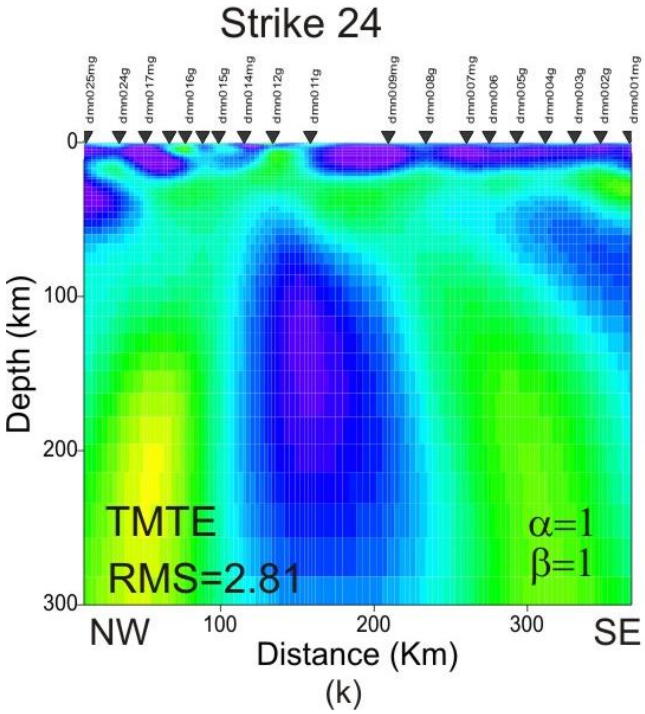
Strike 24
Depth (km)
0
100
200
300
TMTE
RMS=2.81
α=1
β=1
NW
100
200
300
SE
Distance (Km)

(k)

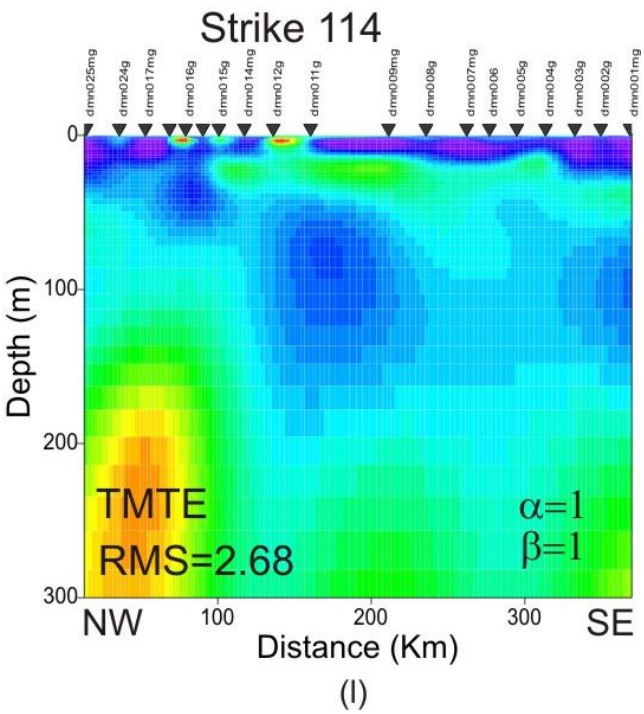
Strike 114
Depth (m)
0
100
200
300
TMTE
RMS=2.68
α=1
β=1
NW
100
200
300
SE
Distance (Km)

(l)

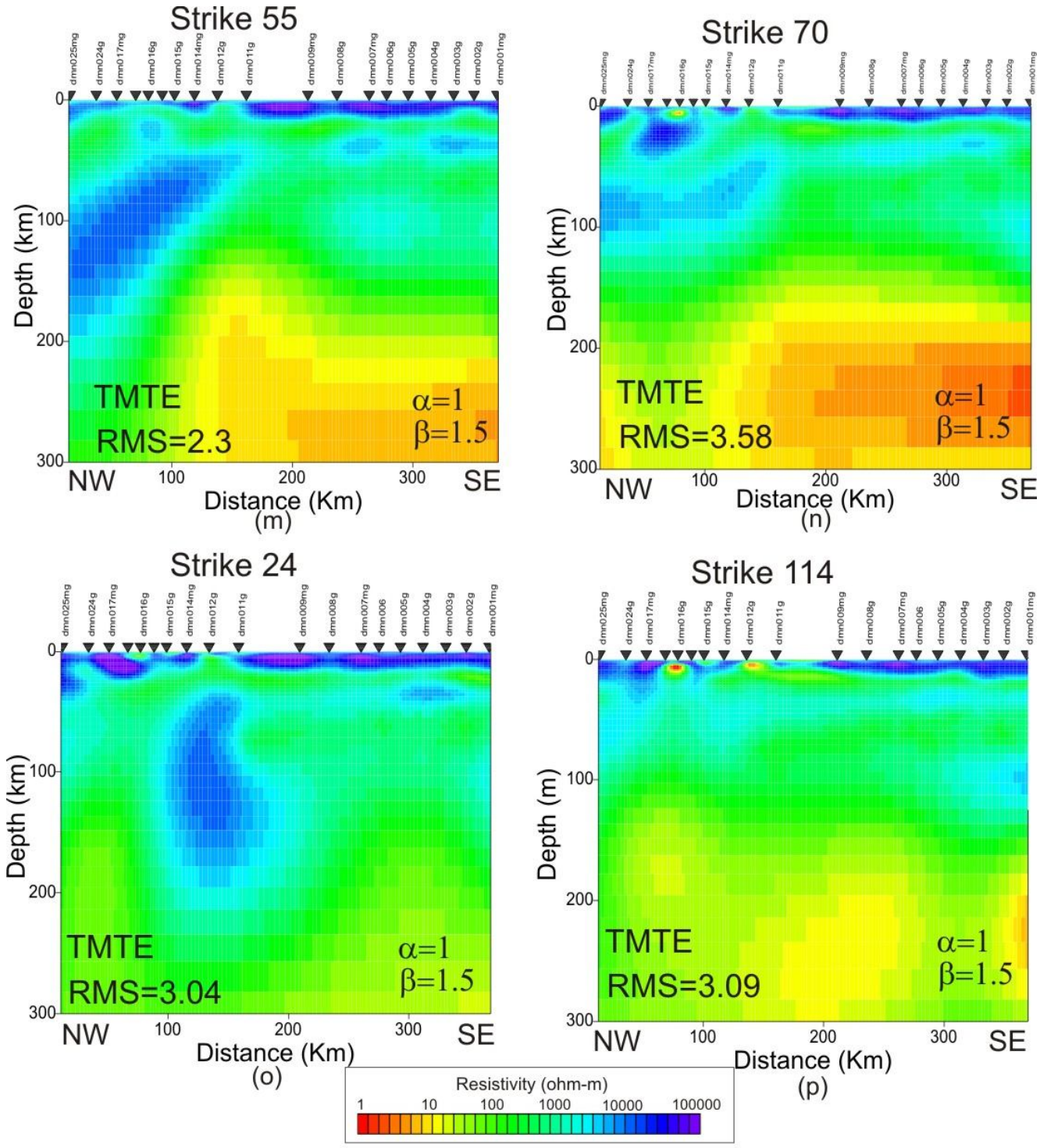

Figure 11: Preliminary models of the MT data at various strike angles, using various data components and variables after 50 iterations. The TM-only data were used with an alpha value of 1 and beta of 1 at strike angle 55° (a), 70° (b), 24°(c), and 114°(d). The TM-only data were used with an alpha value of 1 and a beta value of 1.5 at strike angle 55° (e), 70° (f), 24°(g), and 114°(h), The TM and TE-data were used with an alpha value of 1 and beta value of 1 at strike angle 55° (i), 70° (j), 24°(k), and 114°(l). The TM and TE-data were used with an alpha value of 1 and beta value of 1.5 at strike angle 55° (m), 70° (n), 24°(o), and 114°(p).

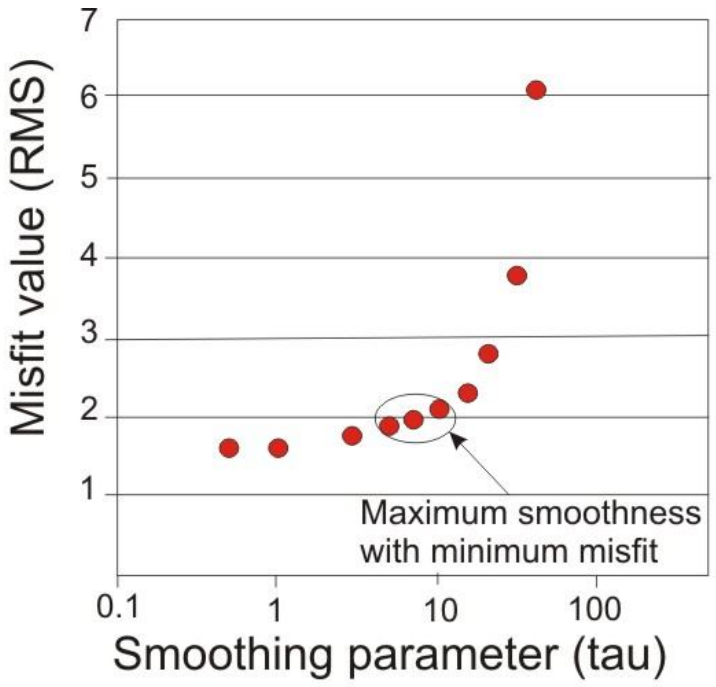

Figure 12: Graph illustrating the trade off between the RMS misfit of the model to the data and the tau value of the inversion. The tau value chosen for the final model is 7.